Phased Acoustic Array Measurements of a 5.75% Hybrid Wing Body Aircraft

Nathan J. Burnside[1] and William C. Horne[2]
NASA Ames Research Center, Moffett Field, CA, 94035

Kevin R. Elmer[3] and Rui Cheng[4]
The Boeing Company, Huntington Beach, CA, 92647

Leon Brusniak[5]
The Boeing Company, Everett, WA, 98204

Detailed acoustic measurements of the noise from the leading-edge Krueger flap of a 5.75% Hybrid Wing Body (HWB) aircraft model were recently acquired with a traversing phased microphone array in the AEDC NFAC 40- by 80-Foot Wind Tunnel at NASA Ames Research Center. The spatial resolution of the array was sufficient to distinguish between individual support brackets over the full-scale frequency range of 100 to 2875 Hz. For conditions representative of landing and take-off configuration, the noise from the brackets dominated other sources near the leading edge. Inclusion of flight-like brackets for select conditions highlights the importance of including the correct number of leading-edge high-lift device brackets with sufficient scale and fidelity. These measurements will support the development of new predictive models.

Nomenclature

AOA	=	Angle-of-attack, degrees
BNS	=	Background noise subtraction
c_s	=	Krueger characteristic dimension, inches
CSM	=	Cross spectral matrix
δ_{KR}	=	Leading-Edge Krueger angle relative the main element, degrees
f	=	Frequency, Hertz
f_d	=	Doppler-shifted frequency, Hertz
FTN	=	Flow-through-nacelle
L_p	=	Sound pressure level, decibels
$L_{p(1ft)}$	=	Sound pressure level normalized to 1 ft from source, decibels
L_{pNorm}	=	Normalized sound pressure level, decibels
M	=	Mach number
PSC	=	Preferred System Concept
Q	=	Dynamic pressure, lb/ft^2
R	=	Propagation distance from leading-edge Krueger mid-span to array center, inches
R’	=	Convected propagation distance from leading-edge Krueger mid-span to array center, inches
St	=	Strouhal number, dimensionless
Θ	=	Emission angle relative to leading-edge Krueger mid-span, degrees
Θ’	=	Convected emission angle relative to leading-edge Krueger mid-span, degrees

[1] Aerospace Engineer, Experimental Aero-Physics Branch, MS 260-1, AIAA Senior Member
[2] Aerospace Engineer, Experimental Aero-Physics Branch, MS 260-1, AIAA Associate Fellow
[3] Acoustics Engineer, MC H017-D335, AIAA Member
[4] Acoustics Engineer, MC H014-D335, AIAA Member
[5] Acoustics Engineer, P.O. Box 3707, MC 0R-116

I. Introduction

THE Environmentally Responsible Aviation (ERA) Project within the Integrated Systems Research Program (ISRP) of the NASA Aeronautics Research Mission Directorate (ARMD) is tasked with the exploration and documentation of vehicle concepts and enabling technologies to mitigate the impact of aviation on the environment. The milestones of the ERA program are to reduce noise, NOx emissions, and fuel burn through new technologies and vehicle concepts. The Boeing proposed Preferred System Concept (PSC) ERA-0009GM Hybrid Wing Body (HWB) concept vehicle was tested as an ERA Project capstone test. The 5.75% HWB model was tested in Arnold Engineering Development Complex (AEDC) 40- by 80-Foot Wind Tunnel (40x80) at NASA Ames. Figure 1 shows the model installed in the wind tunnel along with three locations of the traversing array system.

The ERA capstone test know as ITD-51 was originally planned for the Langley 14x22 Wind Tunnel, however because of a drive motor failure, the test was moved to the 40x80 to maintain ERA milestone deadlines. The 14x22 test entry did not include acoustic measurements because of time and budget constraints. Moving the test to the 40x80 allowed the ERA Project to meet its milestone dates and offered the ability to add acoustic testing to the already planned aerodynamic testing with minimal impact and cost. Data from a previous 3%-scale wind tunnel test of an HWB showed that the noise emitted from a conventional leading-edge slat high-lift system was one of the dominant noise sources since the vehicle configuration benefits from engine shielding[1]. This test also demonstrated that the leading-edge high-lift noise for an HWB configuration could be louder than for previous vehicles due to the higher angle-of-attack needed for landing. Concern about noise generated by a leading-edge Krueger Flap device, drove the design of a traversing array system to capture Krueger noise data from source emission angles of 60° to 120°.

The acoustic objectives of this test were to document the noise field of the HWB leading-edge Krueger for a range of conditions of model attitude and Krueger rigging to support the development of improved noise models. Another objective was to resolve noise sources at the leading edge to associate noise source location and strength with physical details of the model, such as Krueger gaps and brackets.

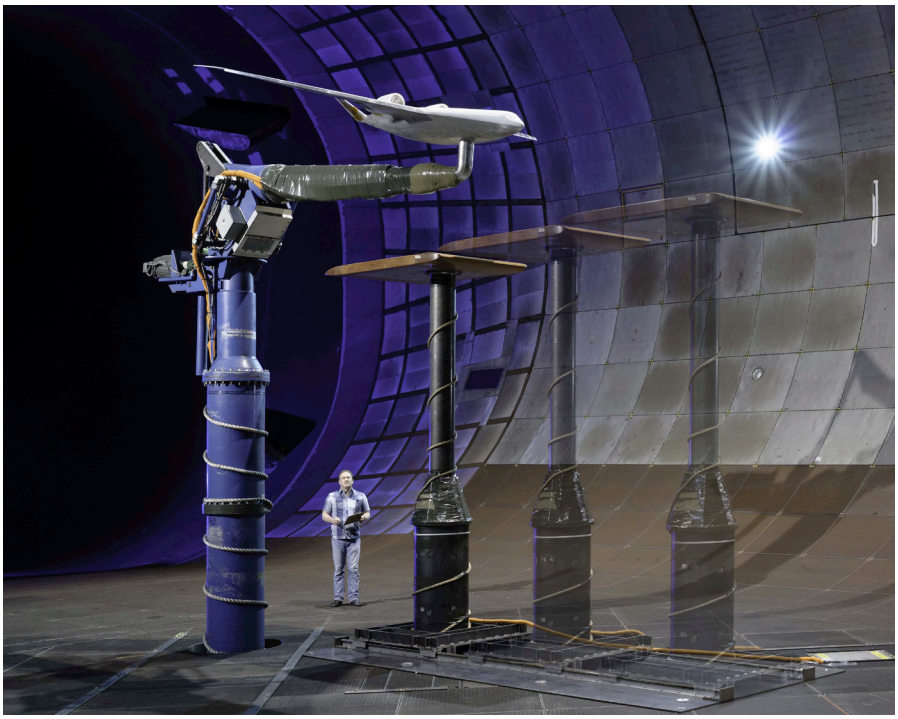

Figure 1. Multiple exposure photo showing the traversing array positions with the HWB model installed.

II. Model

The 5.75%-scale model was outfitted with a 6-component flow-through balance and sting mounted atop a single strut with a pitch mechanism. The model was designed to accommodate aerodynamic testing with flow-through-nacelles (FTN), powered flight-testing with two thrust propulsion simulators (TPS) units, and inlet distortion testing with high-pressure air injector assemblies. FTN, TPS, and ejector testing were conducted during discrete phases of testing and each had their own milestones. Acoustic testing was added to the program shortly before the second entry into the 40x80 and was performed with the FTNs installed. The primary acoustic goal was to measure leading-edge Krueger noise in a number of takeoff and landing configurations.

The deployment angle of leading-edge Kruger flaps were varied along with the trailing-edge position relative to the main element. Leading-edge Krueger deployment angle, δ_{KR}, was varied between 40° and 50°. The gap between trailing edge of the Krueger and the main element was varied during acoustic testing and was denoted by a matrix type notation as shown in Figure 2a. Landing configuration used a 3x3 matrix while takeoff had a 2x2 configuration. A leading-edge Krueger with a 40° deflection and very little gap has the notation 40°(3,3). Two leading-edge Krueger shapes were tested, the aerodynamic baseline and the acoustic Krueger as shown in Figure 2b.

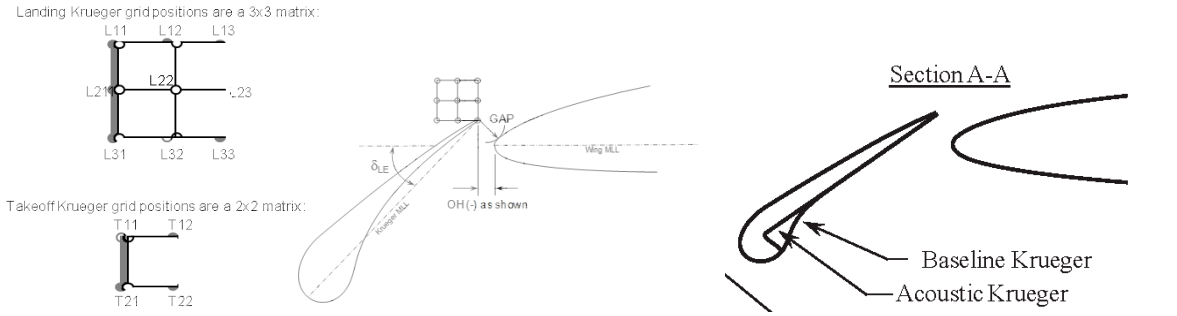

a) Krueger deployment for landing and takeoff. **b) Baseline and acoustic Krueger profiles.**

Figure 2. Leading-edge Krueger geometry.

Along with exposed gaps and edges in high-lift systems, bracket noise has been previously observed as an important component of leading-edge high-lift noise of swept wing aircraft[2]. Brackets for high lift devices are a challenge for wind tunnel model designers because of their complexity on the full size aircraft. The brackets and hydraulic mechanisms must be strong during deployment and fold and stow inside the wing. As a noise source, the small details of a particular bracket design can have significant impact on the spectral level radiated noise. Rapid prototype manufacturing make it possible to achieve realistic features at very small scale, however the brackets on a wind tunnel model must also support the high lift device under a number of load conditions. To further complicate the matter, configuration changes usually involve changing brackets to achieve the different flap or slat positions and angles tested. To simplify model changes, high-lift device brackets are generally highly simplified and are many times larger than a realistic scaled version. In the baseline configuration this model had five structural brackets to support the leading-edge Krueger as opposed to 22 on the proposed flight vehicle.

While this simplification has been made for most wind tunnel models to date, it may not produce the most accurate acoustic representation. To investigate the effect of increasing the size, reducing complexity, and decreasing the number of Krueger brackets 17 flight-like brackets were manufactured to the correct scale with many more details representative of the full size brackets using rapid prototyping. Spacing between the flight-like brackets ranged from 2.08 in to 2.87 inches while the nominal spacing between the structural brackets was 15 inches. The flight-like brackets were mounted in between the structural brackets as shown in Figure 3. Figure 4 shows how different the structural and flight-like brackets were for this test. The structural brackets were typical of a simplified geometry used for many models. Note that the structural brackets were taped because pressure-tube bundles were routed from the Krueger to the wing along the brackets. Flight-like brackets were only tested on one approach configuration; the majority of the testing was conducted with structural brackets. The leading-edge Krueger and brackets were removed for testing in the cruise configuration. More details of the model development can be found in Dickey et al[3].

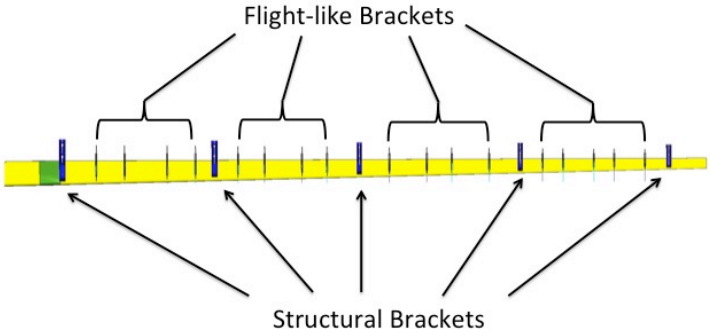

Figure 3. Flight-like Krueger brackets were mounted in between structural brackets to more closely represent the flight vehicle.

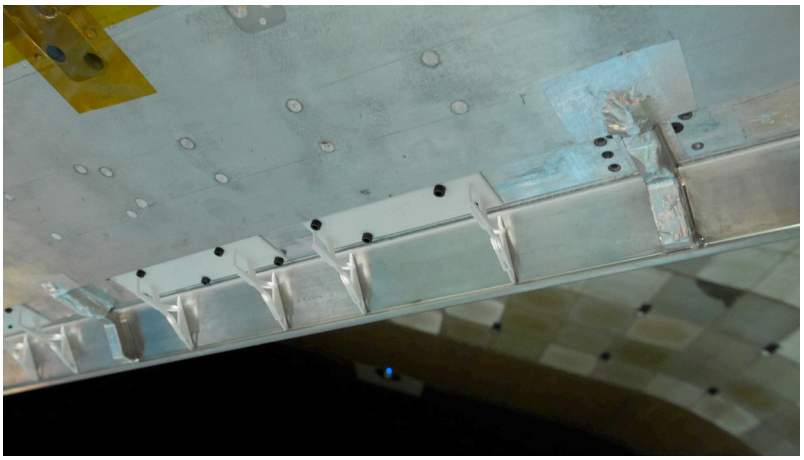

Figure 4. Photo of two structural and six flight-like brackets.

III. Phased Array

A. Traversing Array Design

The phased microphone array was placed into an existing aerodynamic fairing and mounted atop a new traversing array support system. To achieve spatial resolution good enough to resolve the five structural Krueger brackets and to improve signal-to-noise ratio the array needed to be placed as close to the model as possible without interfering with the aerodynamic performance and to remain in the far-field of the individual noise sources. The final decision to acquire acoustic data was made close to the tunnel entry date. A further requirement was that the array fairing not interfere significantly with the model aerodynamic performance, and that the acoustic measurements not adversely impact the aerodynamic phase of the test schedule. The former requirement was validated with extensive CFD analysis and comparison of performance measurements with and without the array present. The latter requirement was met by an efficient stand-alone acoustic data acquisition and processing system developed for numerous prior test programs that acquired detailed acoustic measurements on a non-interference basis for the tests with priority on precision aerodynamic measurements.

The resulting array traversing array support is shown in Figure 1. The array was manually positioned at nominal convected radiation angles of 60˚, 90˚ and 120˚ for an angle of attack (AOA) of 0˚. At 90˚ emission angle, the distance from the array to the wing leading edge varied from 56.89 in. to 111.57 in. as the AOA varied from 0˚ to 30˚.

Array position locations were approximated to provide convected emission angles every 10° for the range of 60° to 120° for a nominal dynamic pressure (Q) of 60 lb/ft^2 or Mach 0.2. At the time of design, the contingency plan to make array measurements with a larger separation distance which dictated a design with hold down locations for tall and short strut designs. The leading-edge Krueger flap was the primary noise source of interest so the center of the array was placed at the mid-span of the leading-edge Krueger, all angles and distances were referenced to this point.

Figure 5 shows the array under the model at a nominal 90° emission angle; it is clear that the array will measure a range of emission angles because of the sweep of the wing. The array positions corresponding to the nominal emission angles are designated with an 'X', i.e., X90 is the position for the nominal 90° flyover angle. Actual emission angles are not preceded by an 'X'. Model angle-of-attack causes the emission angles to change for a fixed array position. Table 1 lists the geometric source emission angles for each of the array positions while Table 2 lists the typical convected emission angles for Mach = 0.2.

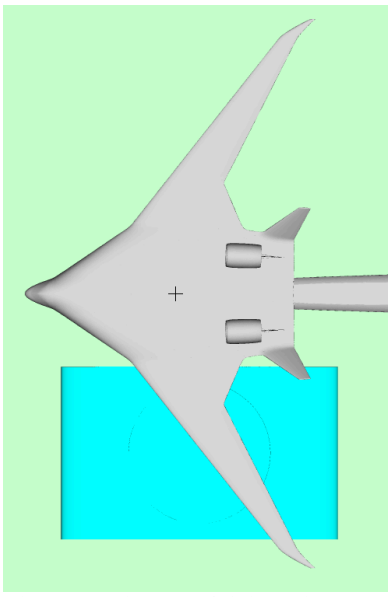

Figure 5. Array fairing in the X90 position under the left hand wing.

Table 1. Unconvected geometric leading-edge Krueger source emission angles.

Geometric Source Emission Angles									
α	0	2	4	6	8	10	12	14	16
X60	65.3°	66°	66.5°	66.8°	67°	67.1°	67.1	67°	66.8
X90	90°	89.1°	88.3°	87.4°	86.5°	85.6°	84.5°	83.8	82.9°
X120	117.4°	115.2°	113.6°	111.2°	109.3°	107.5°	105.7°	104°	102.3°

Table 2. Leading-edge Krueger source emission angle with a Mach 0.2 convection.

Mach 0.2 Convected Source Emission Angles									
α	0	2	4	6	8	10	12	14	16
X60	76.8°	77.5°	78.1°	78.4°	78.6°	78.7°	78.7°	78.6°	78.4°
X90	101.6°	100.8°	99.9°	99.1°	98.2°	97.4°	96.5°	95.6°	94.7°
X120	126.8°	124.9°	123.1°	121.3°	1196°	117.9°	116.3°	114.7°	113.2°

B. Array Pattern Performance

A new 48-element array with a 40-inch diameter pattern was designed for this test. Two nested arrays were designed into the microphone pattern as shown in Figure 6a, however all data presented in this paper were processed using all 48 elements. Figure 6b is a double y-axis plot showing the radius of the 3 dB down contour with solid lines on the left axis and the sidelobe dynamic range with dashed lines on the right axis. The sidelobe dynamic range and resolution is obtained with conventional beamforming, both are significantly improved with advanced beamforming. For a given frequency, decreasing array diameter (using the inner nested array) increases the diameter of the 3 dB down contour but improves the sidelobe dynamic range as would be expected. The close proximity of the array to the noise sources for this test provided a very good signal-to-noise ratio and the small improvement of sidelobe dynamic range did not outweigh the improved resolution when using all 48-elements.

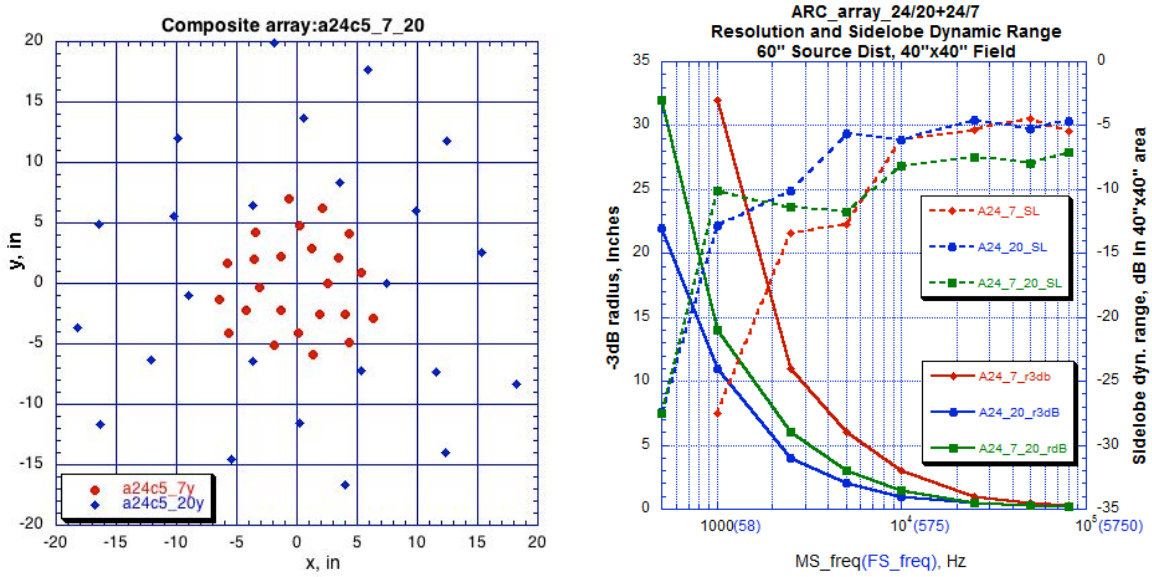

a) Nested array patterns **b) Array Performance**

Figure 6. Phased microphone array pattern and performance. The smaller nested pattern is shown in red, the larger pattern in blue, and green shows the combination of both.

IV. Data Processing

Data processing was conducted using OptiNav's Beamforming Interactive plugin for *ImageJ*. The commercial software has options for many different processing methods from conventional beamforming to the most state-of-the art methods such as Robust Functional Beamforming. A number of custom *Matlab* and Unix scripts allow for automation of the data processing, a necessity for wind tunnel testing. To extract the leading-edge Krueger noise a number of processing methods, techniques, and corrections are performed to achieve the final data. Beamform maps presented in this paper have been corrected with background noise subtraction unless otherwise noted, however no test day corrections were applied. Spectra presented have both background noise subtraction and test day effects removed unless otherwise noted and have been normalized to a 1ft source distance.

A. Background Noise Subtraction

Wind tunnel background noise and noise sources on the model other than the sources of interest can be problematic. Background noise subtraction (BNS) is a method available in the OptiNav software to remove or reduce unwanted noise sources. The method requires a dataset with the unwanted noise sources and another dataset with the desired noise source as well as the unwanted background noise. After the cross-spectral matrix (CSM) for both datasets is computed the background noise CSM is subtracted from the CSM containing the background and desired noise signals. The resultant CSM is used for beamforming to produce source location maps with the undesirable sources removed or reduced.

Because the acoustic focus of this test was to measure the leading-edge Krueger noise, data were acquired with the model in a cruise configuration with no leading-edge device deployed to serve as the background noise points. This data were then subtracted from the landing and takeoff configurations with the leading-edge Krueger deployed. In theory this would remove all sources not associated with the Krueger flaps but in practice not all sources are removed. One particularly troublesome source was a 10 kHz tone generated from the right flow-through-nacelle (FTN). Identification and treatment of this contaminating source will be discussed later, however BNS was used to suppress the tone for some of the data. Figure 7 shows the result of the background noise subtraction. At frequencies below 2 kHz noise associated with the wind tunnel drive system is reduced by 5 dB at the lowest frequencies. The 10 kHz tone associated with the FTN is also reduced by 5 dB but is not eliminated. This result shows that BNS can be used to remove some unwanted noise sources but in practice it is difficult to completely remove a very strong source.

B. Region of Interest

Another useful technique to extract the desired noise sources from the background noise is region of interest (ROI) processing. A polygon is created that outlines the region on interest on the beamform map and only sources within the bounded region are shown in the contour map or integrated into the spectra. ROI processing works well to eliminate background sources that are of similar amplitude to the desired noise sources. If the background noise source is the dominant source in the array image its sidelobes can contaminate the region of interest. Each array position and model attitude required a different region of interest. Figure 8 shows the region of interest for the X90° array position with the model at 14° angle-of-attack.

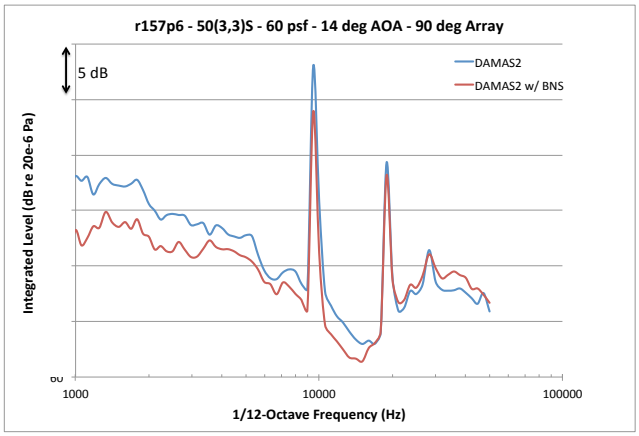

Figure 7. Result of background noise subtraction.

C. Advanced Processing Investigation

Conventional beamforming (CB) is a robust and mature phased-microphone array processing method that provides continuous source distributions with little computational time using modern computers[4]. In recent years however, several new advanced array-processing methods have been developed to improve resolution, increase dynamic range, and reduced sidelobe contamination. Preliminary data were processed using CB during the wind tunnel test to provide quick and robust beamform images to ensure the data system and model were behaving as expected. After the test however, more time was spent optimizing the processing methods for use on the final data. A detailed study of advanced processing methods was completed for a limited set of data using Robust Functional Beamforming[5] (FB), TIDY[6], CLEAN-SC[7], and DAMAS2[8] to determine the best method to process the leading-edge Krueger noise for this test. Advanced beamforming results are highly dependent on a number of input parameters and the actual noise sources present. Below is a discussion of results for this test; comparisons made between methods are not intended as an absolute ranking of processing methods.

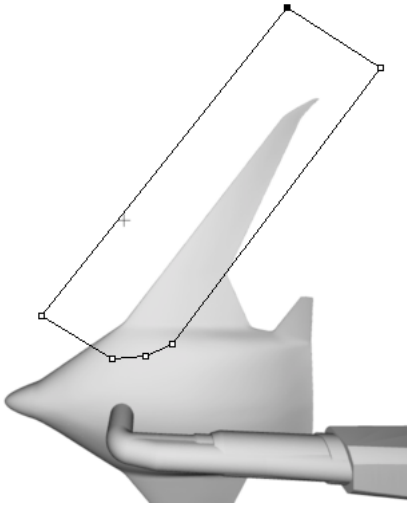

Figure 8. Region of interest for the X90 position at 14° angle-of-attack.

Choosing an advanced array processing method is a tradeoff study to find a method that produces reasonable results with an acceptable computational cost. Peak levels produced with an advanced method should be very close to peak levels with conventional beamforming. Source location with improved resolution is always desirable when analyzing aeroacoustic wind tunnel data. For this trade study a data point acquired at Mach 0.2, α = 14°, and X90 position with the 5 structural and 17 flight-like Krueger flap brackets in a landing configuration with an open gap was used [45°(3,2)]. Data were processed using 1/12-octaves with center frequencies ranging from 250 Hz to 50 kHz. The computational time for each of the methods is listed in Table 3. Of the advanced methods there are clearly two outliers, Functional takes only 4 minutes to complete and TIDY takes 546 minutes to complete. CLEAN-SC and DAMAS2 are a moderate increase in computational time relative to conventional. These times were achieved on a MacPro with a 6-core Intel Xeon E5 CPU running at 3.5 GHz and 64 GB of RAM.

Table 3. Computational cost for various array processing methods.

Conventional	Functional	TIDY	CLEAN-SC	DAMAS2
15 min	4 min	546 min	54 min	55 min

Level accuracy is probably the single most important figure of merit when comparing the various array processing methods. Peak levels for individual sources and integrated levels of multiple sources need to be reasonable and accurate. Figure 9a shows the peak levels in the leading-edge Krueger ROI for each of the methods. Between 4 kHz and 20 kHz all of the methods except for CLEAN-SC produce similar peak levels. TIDY and DAMAS2 are the most closely matched with conventional beamforming throughout the frequency range. The OptiNav software does not integrate the levels for conventional beamforming so the CB peak levels are include with the integrated levels of the advanced methods in Figure 9b. TIDY and DAMAS2 are remarkably similar below 20 kHz.

Source resolution was the last variable considered in the trade study. It was desirable to obtain high enough source resolution to identify noise sources associated with the flight like brackets. Figure 10 to Figure 13 show the results of the resolution study for 4 kHz, 10 kHz, 16 kHz, and 20 kHz. At 4 kHz TIDY, DAMAS2, and CLEAN-SC begin to show many individual bracket noise sources while Functional and Conventional have the bracket sources grouped together appearing as a distributed source. At 10 kHz CLEAN-SC resolves most of the brackets with a few missing while TIDY and DAMAS2 show brackets but some are grouped together as oblong contours. Functional and Conventional begin to show brackets but the long distributed source is still the dominant feature. By 16 kHz TIDY, DAMAS2, and CLEAN-SC show sources at all of the brackets while Functional and Conventional begin to resolve most of them. By 20 kHz all five methods clearly show individual brackets, however the spot size for CLEAN-SC makes it difficult to see the sources.

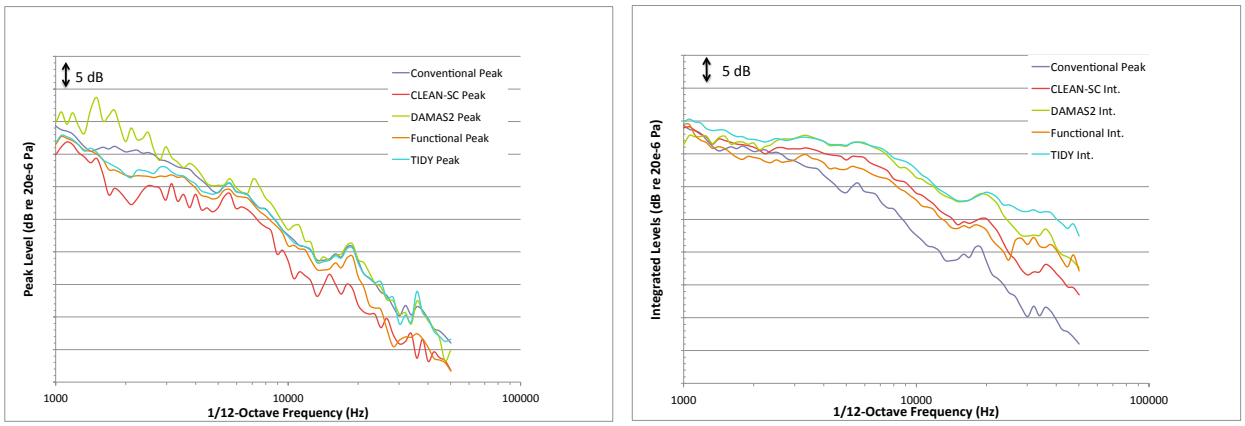

a) Peak levels **b) Integrated levels**

Figure 9. Comparison of peak and integrated levels for the processing method trade study.

Source resolutions for TIDY, CLEAN-SC, and DAMAS2 were sufficient to isolate the individual flight-like brackets at frequencies as low as 4 kHz. Peak levels produced by TIDY and DAMAS2 were the most closely matched with Conventional beamforming and CLEAN-SC did not seem to match very well. Below 20 kHz TIDY and DAMAS2 produce almost identical integrated levels giving confidence in those methods. Between DAMAS2 and TIDY, using this data set and processing parameters, DAMAS2 had the best balance of computational time and level accuracy and was chosen as the processing method for the data discussed in the results section of this paper.

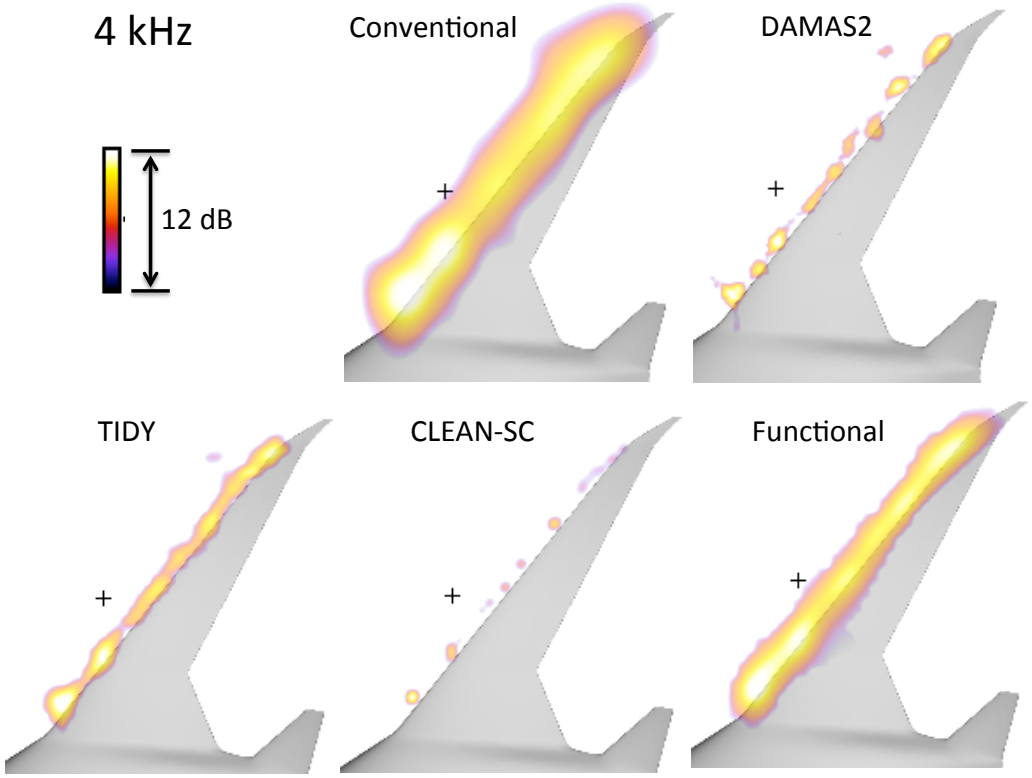

Figure 10. Processing method comparison at 4 kHz. All images have an independent 12 dB range.

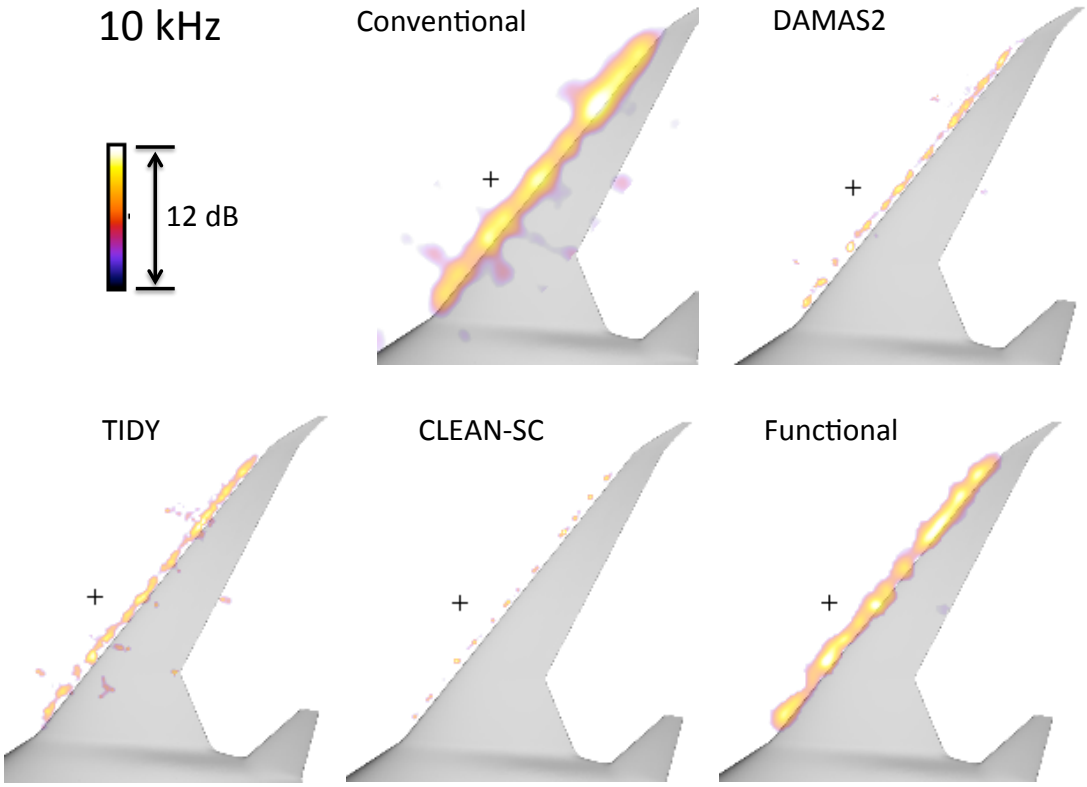

Figure 11. Processing method comparison at 10 kHz. All images have an independent 12 dB range.

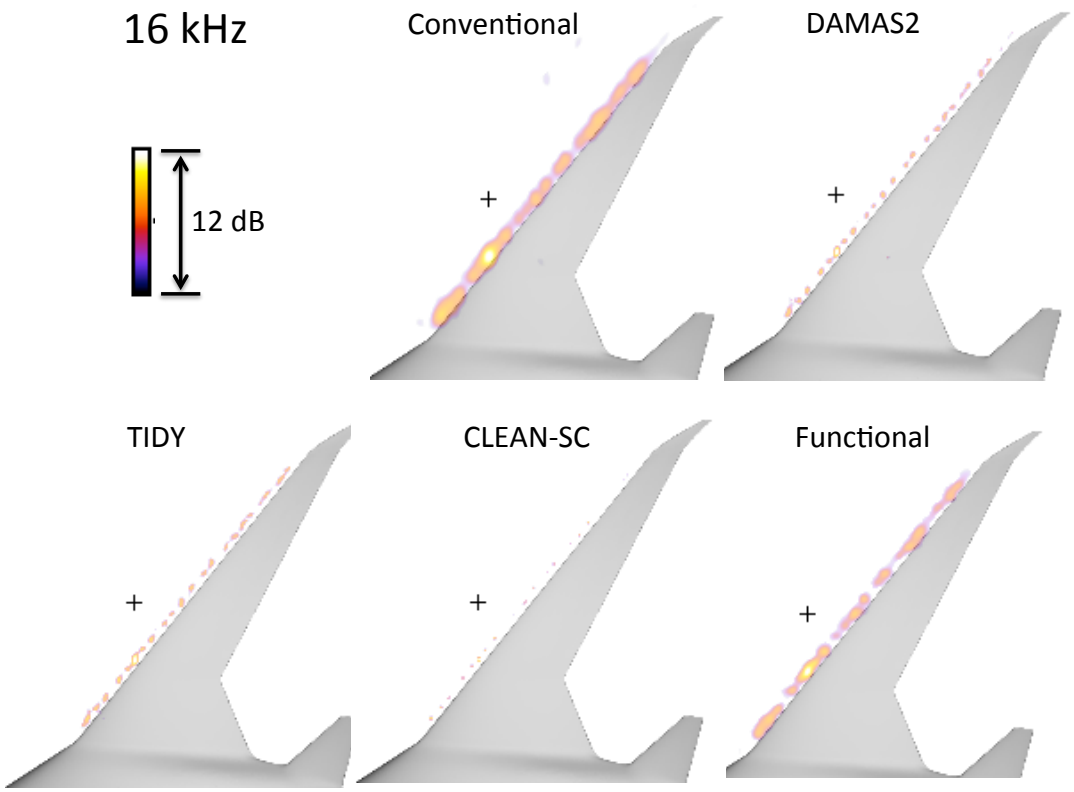

Figure 12. Processing method comparison at 16 kHz. All images have an independent 12 dB range.

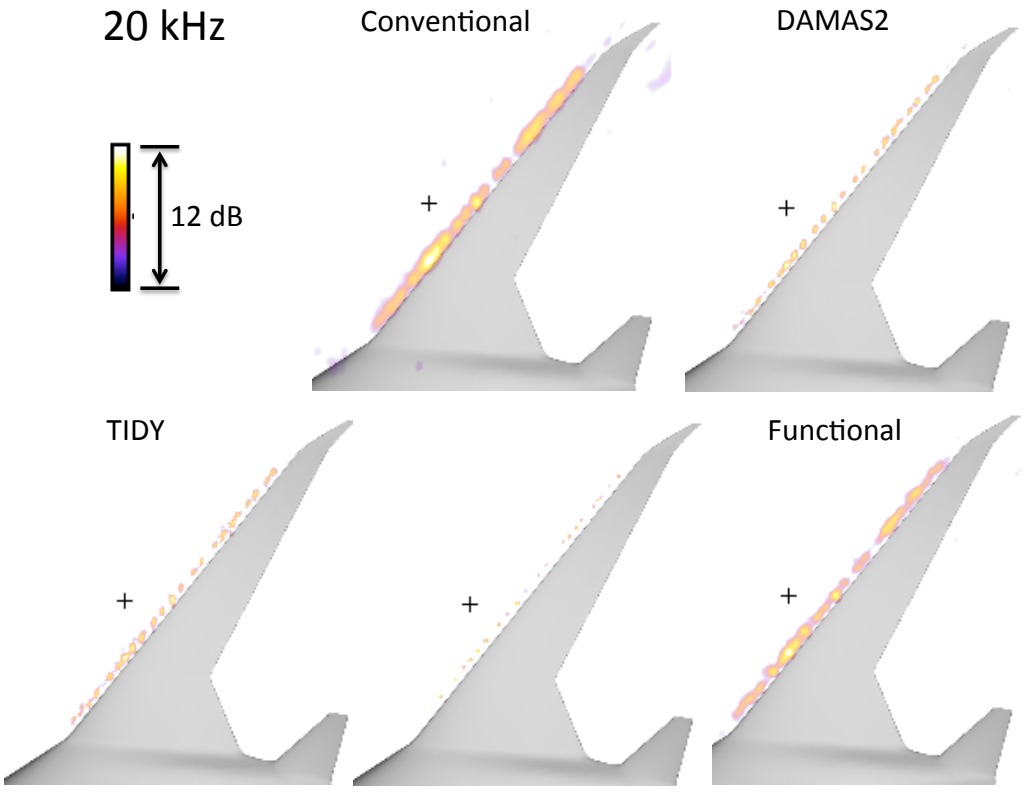

Figure 13. Processing method comparison at 20 kHz. All images have an independent 12 dB range.

D. Sensor and Test Day Corrections

Several corrections are applied to the spectra derived from integrating the beamform maps to remove the test day, microphone, and windscreen effects. The corrections described below are incorporated into the integrated array spectra. Corrections to the data require information about the location of the source, receiver, and the intermediate freestream conditions between the two. Convected emission angle, Θ' and convected propagation path, R′ are used to account for the moving fluid media[9]:

$$\Theta' = \cos^{-1}\left[M\sin^2\Theta + \cos\Theta\sqrt{1-M^2\sin^2\Theta}\right], \tag{1}$$

where Θ is the geometric angle from source to receiver and M is the Mach number of the flow. R′ is the convected propagation distance and is calculated as:

$$R' = \frac{R}{-M\cos\Theta + \sqrt{1-M^2\sin^2\Theta}}, \tag{2}$$

where R is the geometric propagation path from source to receiver.

1. *Microphone Freefield Response Effect*

The G.R.A.S. 40BF freefield microphones used in the array do not measure a true pressure field when placed into a flat plate. The diaphragms are designed to have a lower pressure response as frequency increases to minimize the effects of the microphone on the measured pressure field. When placed in a flat plate this response is not needed because the plate creates a pressure field doubling, resulting in a uniform 6 dB increase in amplitude. The microphone freefield response, H_{FF} is approximated using a 9th order polynomial curve fit of the measured response and was used to remove the freefield response:

$$\begin{aligned} H_{FF}(f) &= 0.46888 - (1.3249\times10^{-4})f \\ &+(2.8876\times10^{-6})f^2 - (9.0321\times10^{-13})f^3 \\ &+(1.2855\times10^{-17})f^4 - (1.0181\times10^{-22})f^5 \\ &+(4.8886\times10^{-28})f^6 - (1.4977\times10^{-33})f^7 \\ &+(2.9289\times10^{-39})f^8 - (2.9285\times10^{-45})f^9, \end{aligned} \tag{3}$$

where f is frequency.

2. *Kevlar Directional Effect*

The Kevlar screen used to suppress the boundary layer noise over the face of the array increases the signal-to-noise ratio significantly[10], however it also affects the measured data and corrections are needed. An in-situ calibration was performed in the 40x80 over the emission range of the phased array with a broadband speaker source attached to mid-span leading-edge of the left hand wing. The test was repeated with the Kevlar screen removed to develop a calibration. Figure 14 shows the frequency and emission angle dependent results. For emission angles and the frequency range of interest in this study, the correction varied between a minimum of -1.5 dB to a maximum of +5 dB. As with all corrections presented in this report the correction is added to the data.

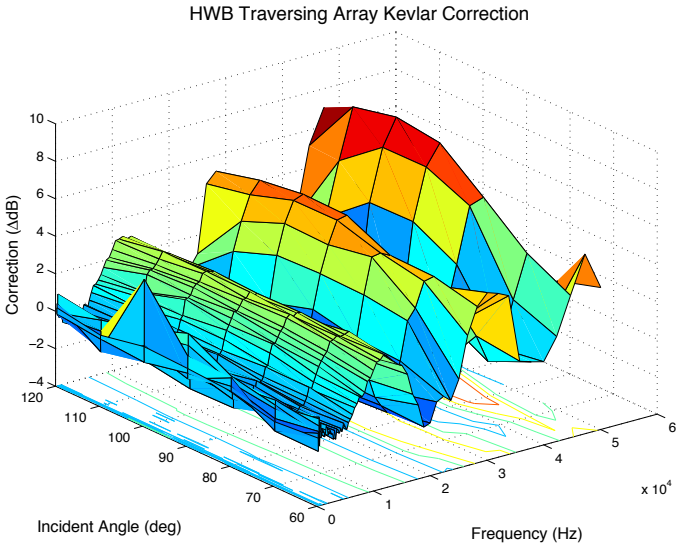

Figure 14. Kevlar correction measured in-situ with a wing mounted broadband noise source.

3. Atmospheric Attenuation and Spherical Spreading

Corrections for attenuation due to atmospheric attenuation were applied using standard equations developed by Shields and Bass and are dependent on static pressure, static temperature, relative humidity, and Doppler-shifted frequency[11]. Doppler-shifted frequency, f_d is calculated:

$$f_d = \frac{f}{1 - M\cos\Theta'}, \tag{4}$$

where f is frequency, M is Mach number and Θ' is the convected emission angle. Effects of spherical spreading were removed and all spectra were normalized to a distance of 1 foot from the source:

$$L_{p(1ft)} = 20\log_{10}\left(\frac{R'}{12}\right), \tag{5}$$

where R′ is the convected source distance. The 12 in the denominator normalizes to a unit distance of 1 foot because the convected distance is measured in inches. Microphone measurements made in a flat plate are corrected for pressure doubling by subtracting 6 dB. Figure 15 is a summary plot of typical corrections applied for nominal conditions, each correction is added to the 1/12-octave spectra.

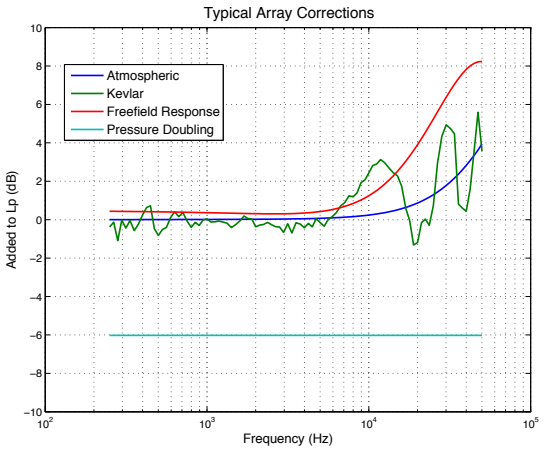

Figure 15. Summary of typical array corrections applied to data.

V. Test Matrix

Although the CFD analysis showed the presence of the acoustic array had little effect on the lift, drag, and pitching moment of the model, it was deemed prudent to test with and without the acoustic array present, primarily for making direct aerodynamic comparisons of data collected at the Langley 14- by 22-Foot Subsonic Tunnel and the AEDC NFAC 40- by 80-Foot Wind Tunnel at NASA Ames Research Center. Therefore acoustic testing was independent of the aerodynamic testing in the FTN configuration, although aerodynamic data were collected during the acoustic portion of the test. The initial test matrix for acoustic testing consisted cruise configurations (needed for BNS), as well as two takeoff and two landing configurations, which were, used in the aerodynamic performance assessments of the PSC. However, test priorities were adjusted to diagnose and eliminate the FTN rake tone, so only the PSC takeoff configuration was tested. Also, the planned angle-of-attack and sideslip sweeps were reduced due to test time and balance force limits being reached for certain testing conditions. Table 4 shows the test matrix for which acoustic data were collected.

Table 4. Summary of acoustic test matrix (repeated at X60, X90, X120 array positions).

Cruise Configuration
Baseline data: α sweep (0°,4°, 8°, 10°, 12°, 14°, 16°, 20°) at β = 0° / α sweeps at -5°≤ β ≤ +10°
Effect of Q variation Q = 20, 40, 50, 60 psf
Landing Configuration δ_{KR} = 40°(3,3) Sealed Krueger
Baseline aero data: α sweeps at β = 0° / α sweeps at -5°≤ β ≤ +10°
Effect of well covers
Effect of elevon deflection (left side only)
Effect of Q variation Q = 20, 40, 50, 60 psf
Landing Configuration δ_{KR} = 45°(3,2)
Baseline aero data: α sweeps at β = 0°, Q=60 psf
Effect of Krueger design (baseline and acoustic)
Effect of Krueger trip dots
Effect of Krueger flight-like brackets
Takeoff Configuration δ_{KR} = 40°(1,1)
Baseline aero data: α sweeps at β = 0°
Effect of Q variation Q = 10, 20, 40, 60 psf
Two additional array positions (X142 and X27)

The analysis thus far has focused primarily on the data processing methods and most relevant conditions of the PSC assessments, specifically background noise, benefit of a sealed Krueger configuration, and the influence of both structural and flight like brackets.

VI. Experimental Results

A. Background Noise

Because acoustic measurements were added so late in the planning process the model support configuration was not ideal for acoustic measurements. A dedicated acoustic test would have enclosed the pitch head mechanism and wiring bundles in an aerodynamic fairing. Attempts were made to cover the wiring bundles in close proximity to the model with tape as shown in Figure 1. Minimizing the distance between phased array and the model improved the signal-to-noise ratio, however there was still some data contamination so it is important to understand these sources. Methods such as background noise subtraction and region of interest processing further minimize the background noise contamination.

1. Strut and Sting Noise

For array positions X60 and X90 there was sufficient spacing between the model support and the array to provide very good signal-to-noise ratio. However in the X120 position the close proximity to the model support interfered some in configurations with low leading-edge Krueger noise. Cable bundles on the sting were taped over to minimize noise however a few times during testing the tape came loose creating a noise source. ROI processing eliminates the strut and sting noise sources and their associated sidelobes were not a problem.

2. Drive Noise

Below 1 kHz drive noise and its sidelobes contaminate the Krueger ROI as shown in Figure 16 where the noise contours appear off body and are clearly not associated with the Krueger flap. Figure 7 shows that a drive noise reduction of as much of 5 dB is obtained using BNS, however wing noise sources such as tip noise, which is common to both the cruise and high-lift configurations, are also removed.

3. Flow-through-nacelle

The most troublesome background noise source however, turned out to be a measurement rake in the right flow-through-nacelle. A very strong tone at 10 kHz and its associated harmonics contaminated the data for the majority of the test as shown in Figure 7. The noise generating mechanism for the tone was difficult to locate because the source location appeared to be on the bottom of the model near the trailing edge of the horizontal tale area. Several attempts to treat various model features in this area did not eliminate the contaminating source. The origin of the noise source turned out to be an instrumentation rake in the FTN on the right side of the vehicle. While the array did not have a direct view of the FTN, the noise may have been propagated downstream by the freestream flow and scattered by the trailing edge of the FTN and airframe. Once the origin of the source was located, placing a porous filter material in the nacelle ahead of the rake eliminated the noise as shown in Figure 17. Source contours in Figure 18a show that the five structural brackets are the dominate noise source at 9 kHz, however at 10 kHz the untreated FTN source dominates by 19 dB as shown in Figure 18b where the dynamic range is the same but the peak level has increased by 19 dB. ROI processing of the leading-edge Krueger ignores the FTN source, however its associated sidelobes are still 10 dB above the bracket noise as shown in Figure 18c. Treatment of the FTN source eliminates the tone without affecting the other noise sources as shown in Figure 18d.

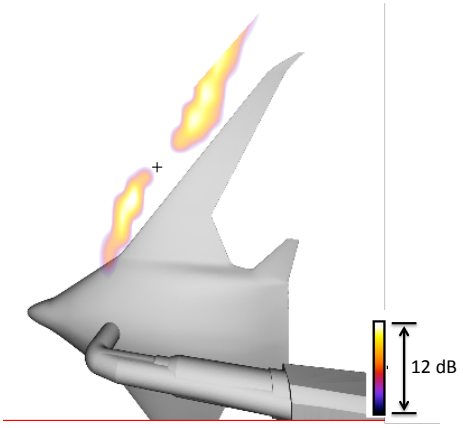

Figure 16. Sidelobes from drive noise at 710 Hz.

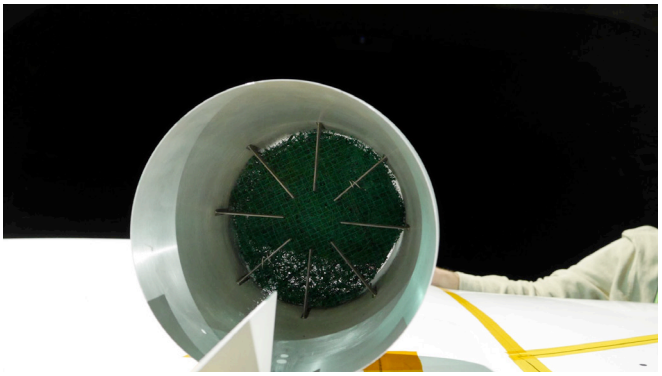

Figure 17. Filter material placed in the right-hand FTN, looking upstream.

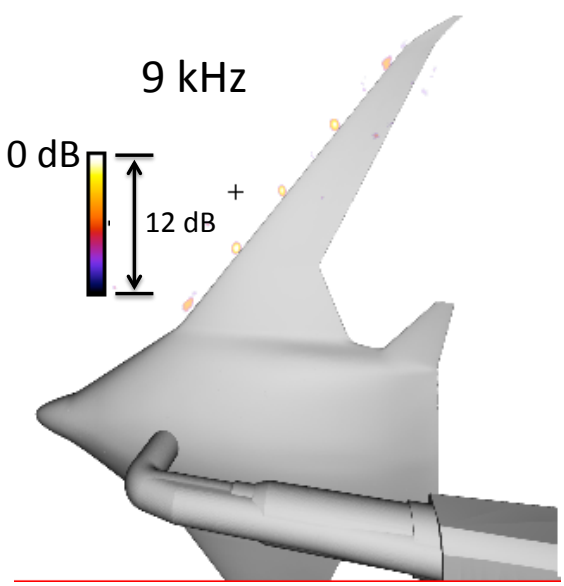

a) **Structural brackets are the dominate source at 9 kHz.**

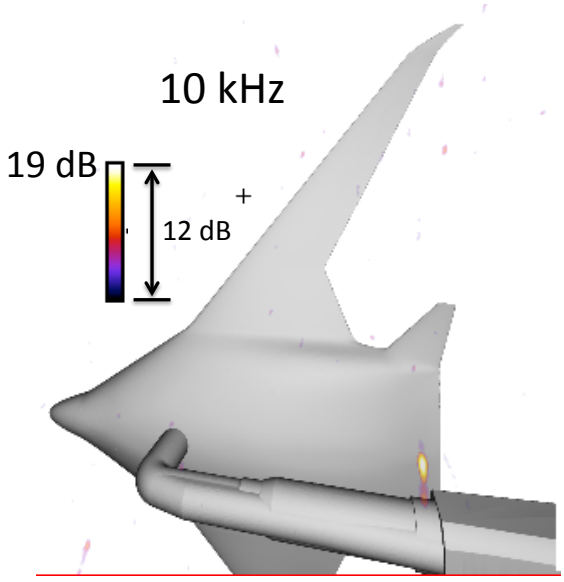

b) **At 10 kHz the FTN tone dominates the noise field by 19 dB.**

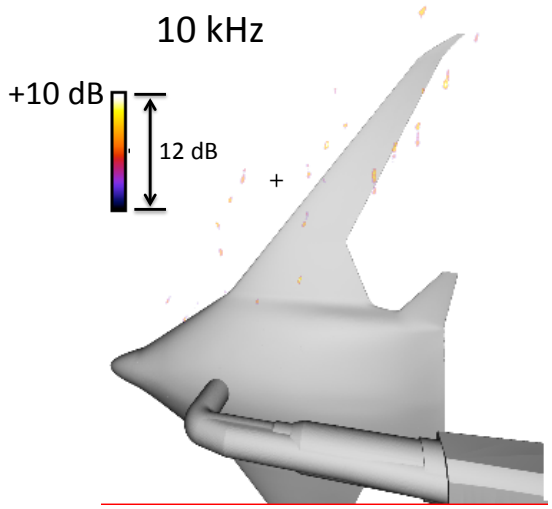

c) **ROI processing eliminates the main source but the sidelobes are 10 dB above the brackets.**

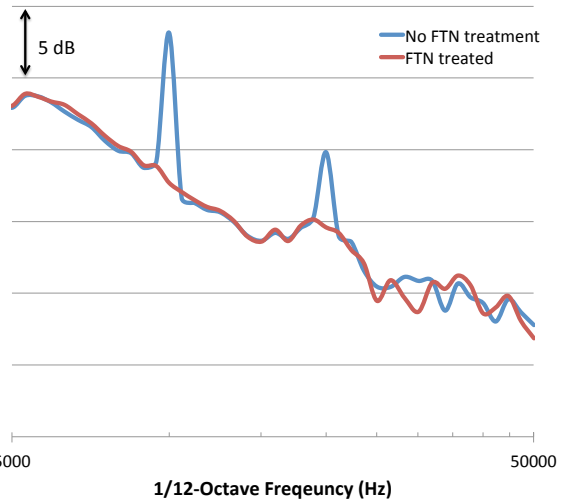

d) **FTN treatment eliminates the tones but ROI processing alone integrates the sidelobe energy.**

Figure 18. Effects of flow-through-nacelle noise.

B. Krueger Brackets

As shown previously, array resolution was sufficient to distinguish between structural and flight-like brackets. Direct comparison between structural only and structural and flight-like brackets was performed for Mach 0.2 over a range of angle-of-attack from 0° to 20° for the X90 and X120 array positions with the model in landing configuration and a 45°(3,2) leading-edge Krueger configuration. Figure 19 shows source location images for six frequencies ranging from 3 kHz to 20 kHz with an angle-of-attack of 14°. At the lowest frequency of 3 kHz, source location images look similar, however the structural and flight-like configuration begins to have some elongated

sources. At 5 kHz the structural and flight-like bracket configuration clearly shows noise sources in between the structural brackets but they are elongated and somewhat connected like a distributed source would appear. As frequency increases the flight-like brackets become clearly visible as distinct compact sources. Integrated spectra of the two configurations show flight-like brackets have more influence as angle-of-attack increases as shown in Figure 20 (note that the convection angle changes as angle-of-attack changes). At the optimized landing angle-of-attack of 14°, addition of the flight-like brackets adds about 5 dB to the majority of the spectrum. Moving the array downstream to the X120 position shows almost identical results as shown in Figure 21 and Figure 22. The 45°(3,2) leading-edge Krueger configuration has a sizable gap between the Krueger and main element likely increasing both the velocity and volume of flow past the brackets.

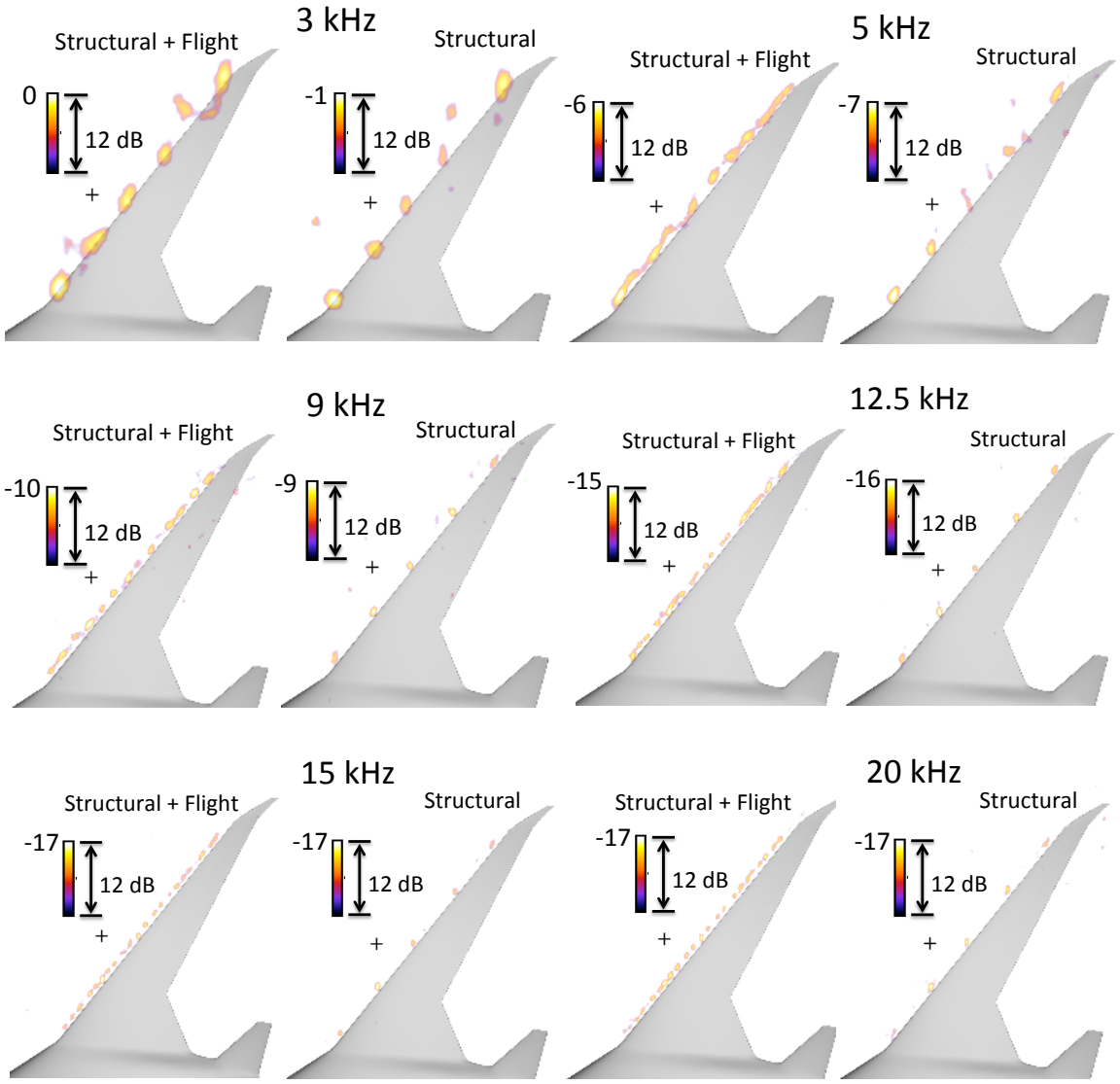

Figure 19. Influence of flight-like brackets at various frequencies: landing, 45°(3,2), Θ' = 95°, α = 14°, M = 0.2. Relative amplitudes are referenced to the peak value in the 3 kHz flight-like bracket beamform map.

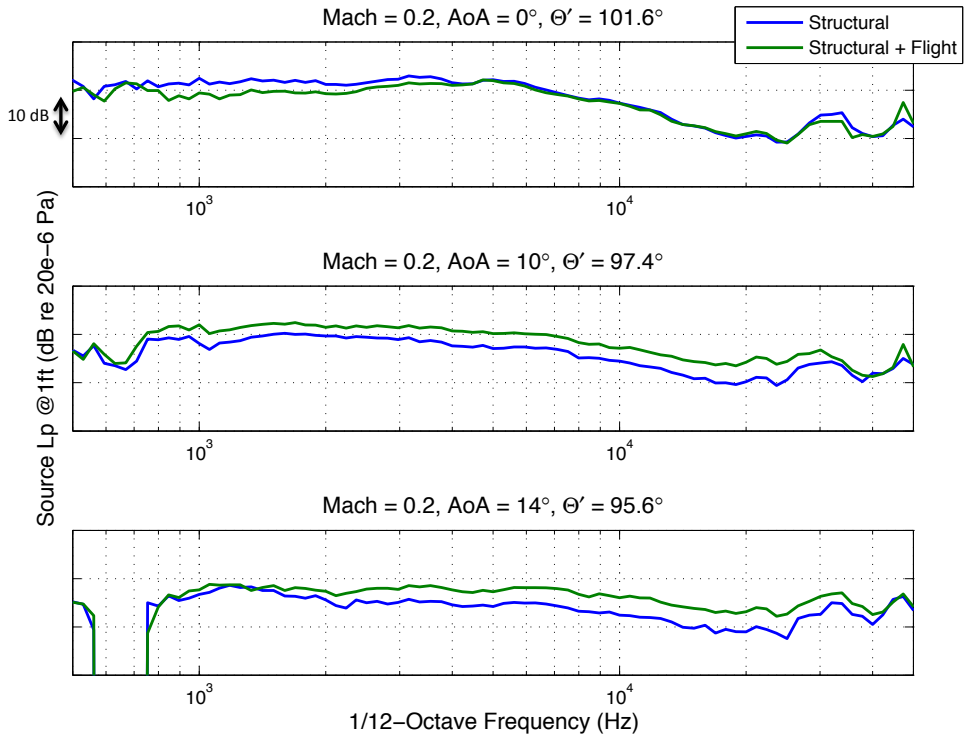

Figure 20. Angle of attack dependence for flight-like bracket influence: landing, 45°(3,2), X90 array position, M = 0.2.

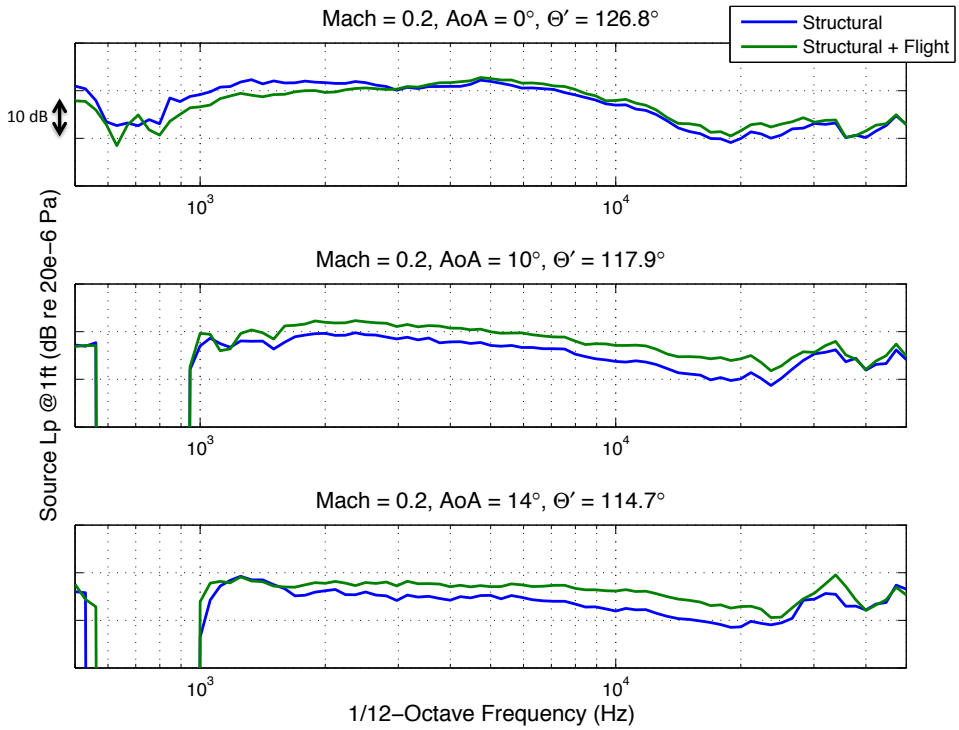

Figure 21. Angle of attack dependence for flight-like bracket influence: landing, 45°(3,2), X120 array position, M = 0.2.

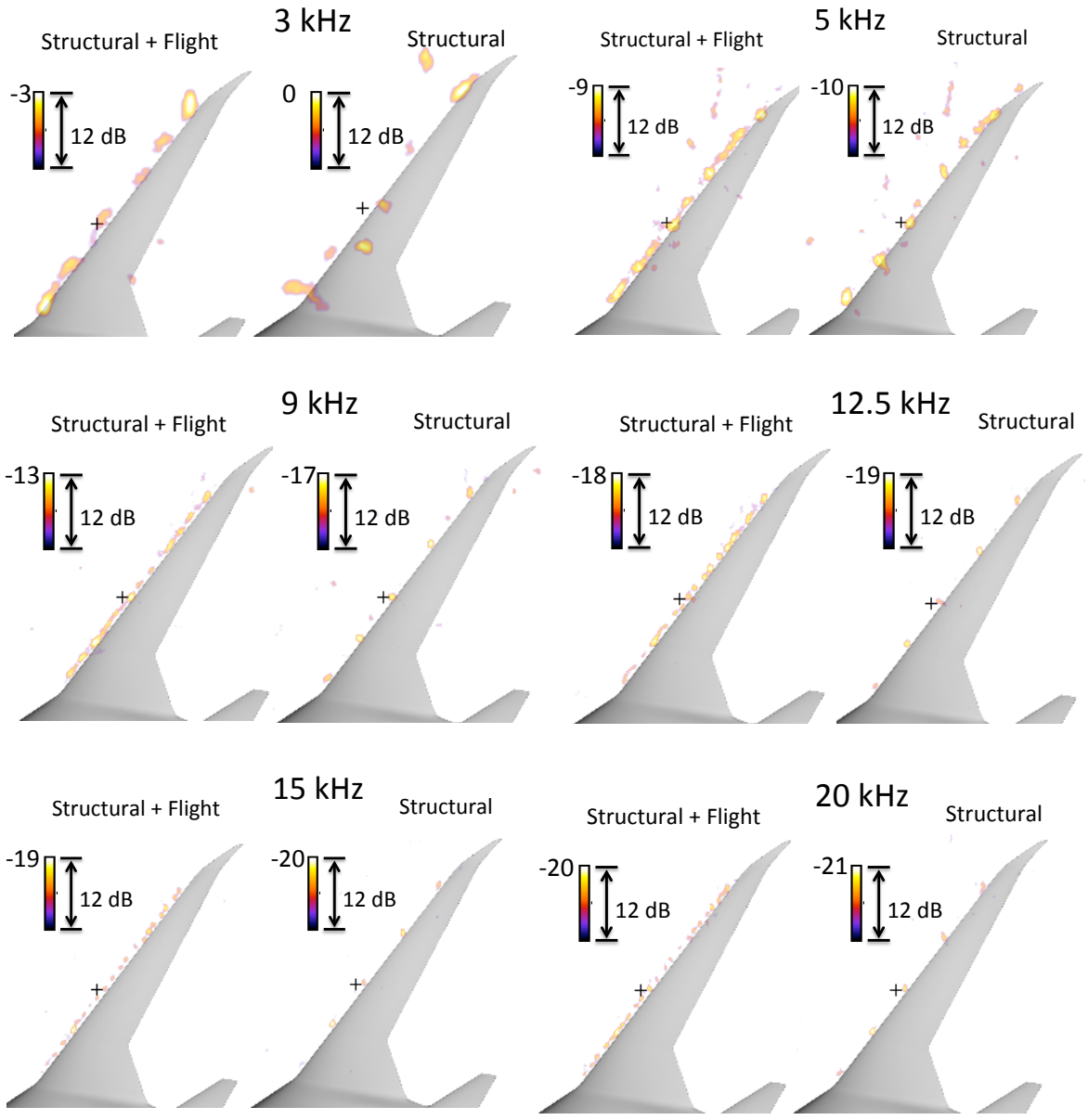

Figure 22. Influence of flight-like brackets at various frequencies: landing, 45°(3,2), Θ' = 118°, α = 14°, M = 0.2. Relative amplitudes are referenced to the peak value in the 3 kHz flight-like bracket beamform map.

C. Krueger Gap

The dominating noise sources for all configurations tested were the Krueger structural or flight-like brackets at most angles-of-attack. Limited gap noise was observed for angles-of-attack of 18° and larger for the 40(1,1) takeoff configuration with structural brackets only at lower frequencies. Figure 23 shows a distributed gap noise source at frequencies below 6 kHz. Figure 24 shows that gap noise makes a significant contribution to the overall leading-edge noise at 18° angle-of-attack.

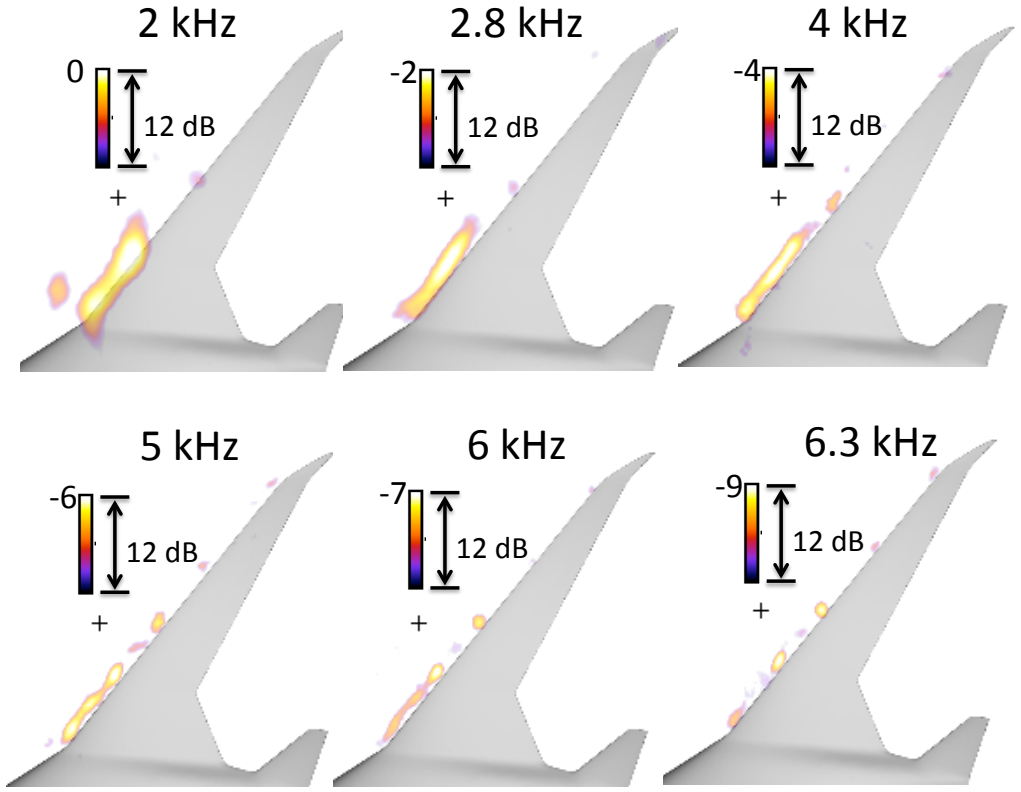

Figure 23. Krueger gap noise at lower frequencies: takeoff, 40°(1,1), Θ' = 95.6°, α = 18°, M = 0.2.

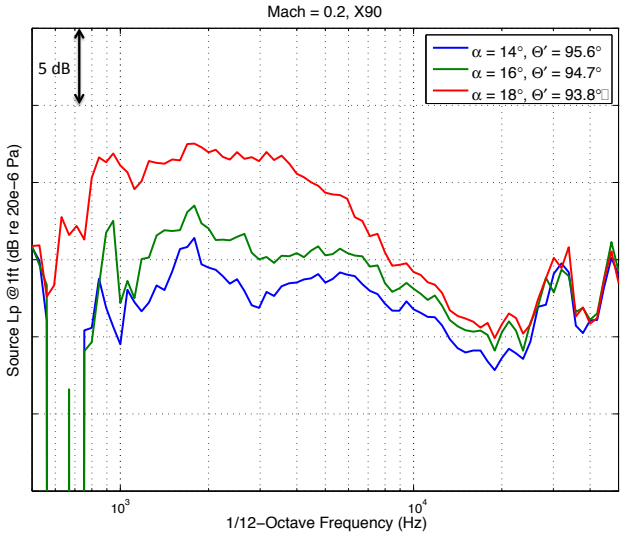

Figure 24. Krueger gap noise is present at higher angle-of-attack: takeoff, 40°(1,1), M = 0.2, X90.

In addition to varying the Krueger gap, a completely sealed configuration was also tested. The landing 50°(3,3) configuration was tested with and without tape sealing the upper surface between the leading-edge Krueger and the main element. At a low angle-of-attack of 0° sealing the Krueger gap reduces the noise in the neighborhood of 2

kHz by as much as 10 dB as shown in the top plot of Figure 25. It is important to ignore the tone at 10 kHz and its harmonics because there was no FTN treatment for this data and BNS was not applied. As angle-of-attack increases the overall noise levels are reduced and begin to approach the noise measured in the cruise configuration although reduction is still observed at 2 kHz. The 50°(3,3) configuration has a very small gap, which is most likely why the overall noise for both the sealed and unsealed gap approach the cruise noise levels at the approach angle of 14°.

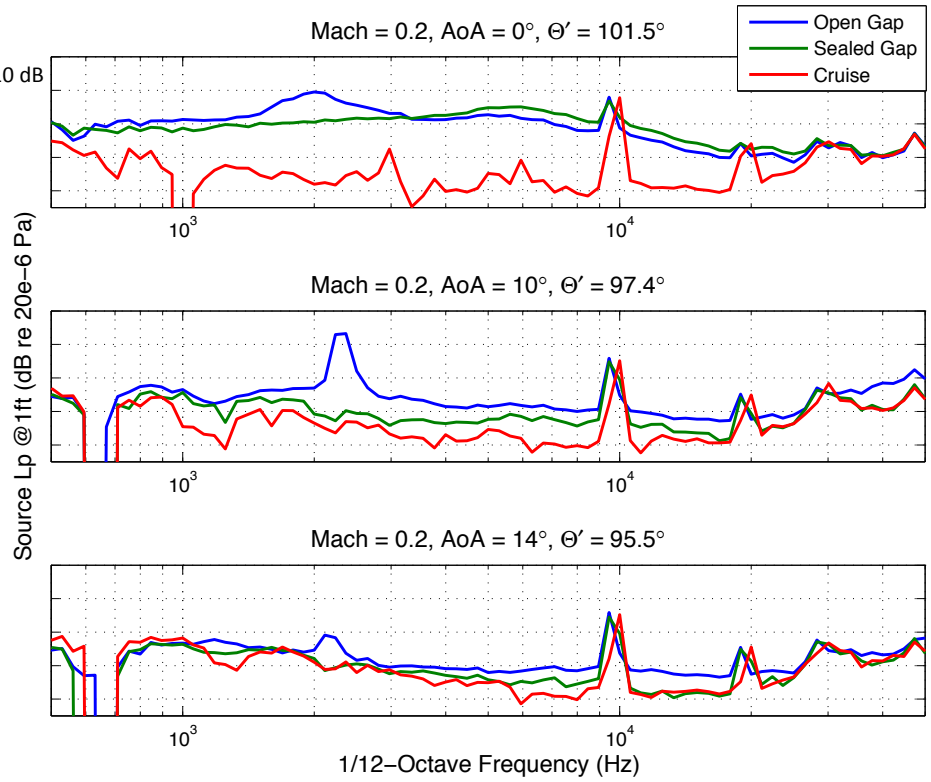

Figure 25. Effect of sealing the Krueger gap: landing, 50°(3,3), X90, M = 0.2.

D. Velocity Scaling

Mach sweeps from M = 0.117 to M = 0.205 were performed for the takeoff Krueger configuration of 40°(1,1) at the three default array positions. Data were normalized using a 5th power scaling:

$$L_{Pnorm} = L_{p(1ft)} - 50\log_{10}\left(\frac{U_{\inf}}{U_{ref}}\right), \tag{6}$$

where $L_{p(1ft)}$ is the distance normalized sound pressure level, U_{inf} is the freestream velocity, and U_{ref} is a nominal reference velocity (100 ft/s). Strouhal number was used as the dimensionless frequency, defined as:

$$St = \left(\frac{fc_s}{U_{\inf}}\right), \tag{7}$$

where f is the model frequency and c_s is the Krueger characteristic dimension (0.134 ft). With the exception of the lowest velocity a 5th power scaling causes the data to collapse within 3 dB between St = 1 and St = 10 as shown in Figure 26.

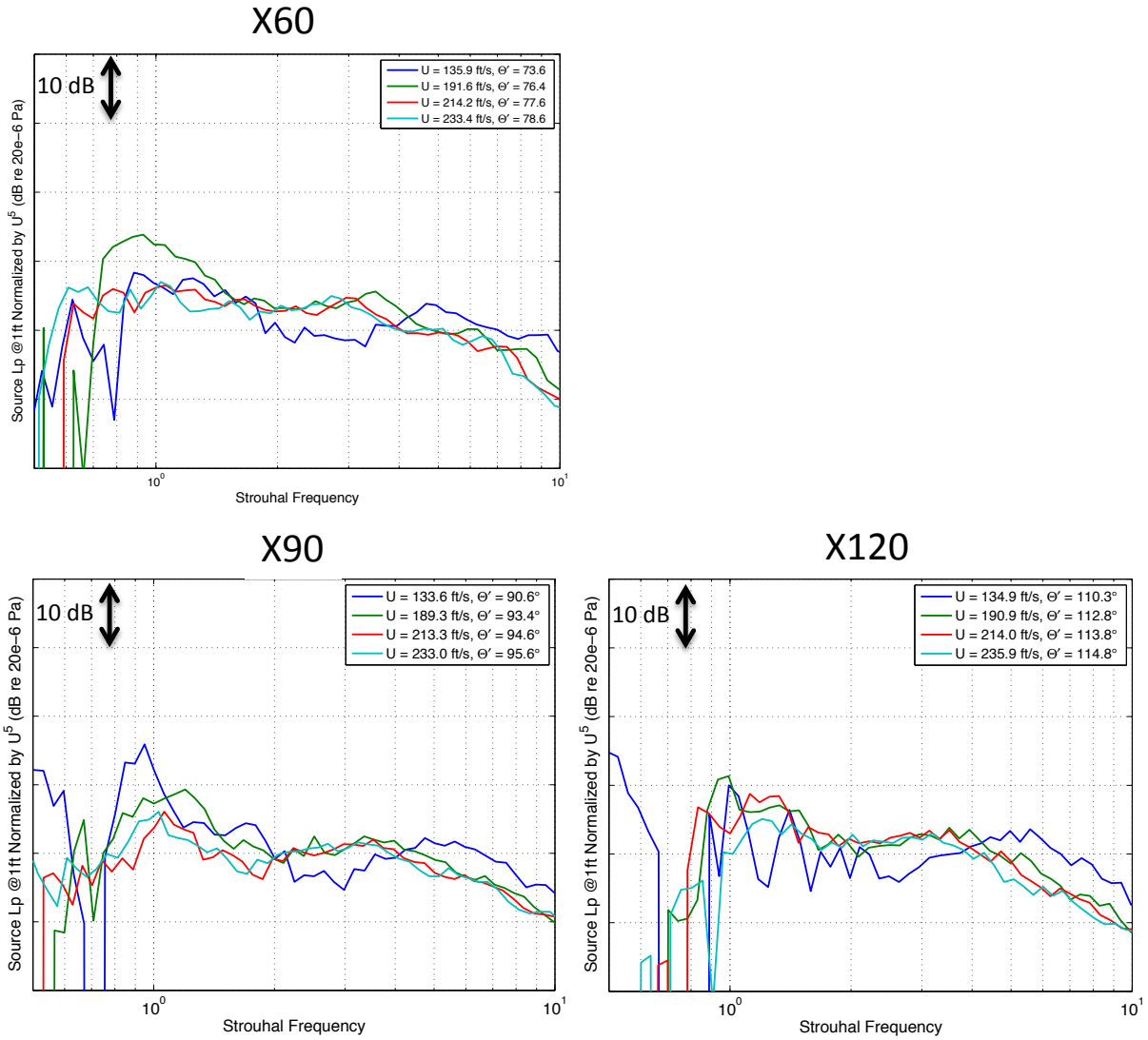

Figure 26. Velocity scaled data for three different array positions: takeoff, 40°(1,1), unsealed gap, α = 14°.

E. Angle of Attack Dependence

Test time was limited so angle-of-attack sweeps were rather course and data acquisition was optimized around the anticipated approach and takeoff angles. Balance limits due to dynamic model loading prevented data acquisition at angles beyond 16° for most of the testing. Angle-of-attack sweeps were performed for most model configurations and flow conditions, however a detailed study was performed for the landing sealed-gap 50°(3,3) configuration. Results from the angle-of-attack study show that the leading-edge Krueger noise decreases as angle-of-attack increases up to 14° as shown in Figure 27. The initial decrease in noise is rather rapid and occurs by 8° for the X90 and X120 array positions and by 4° for the upstream position of X60. This study however is in not complete because it does not include data above 14°; balance load permitting it would have been ideal to acquire data all the way to stall.

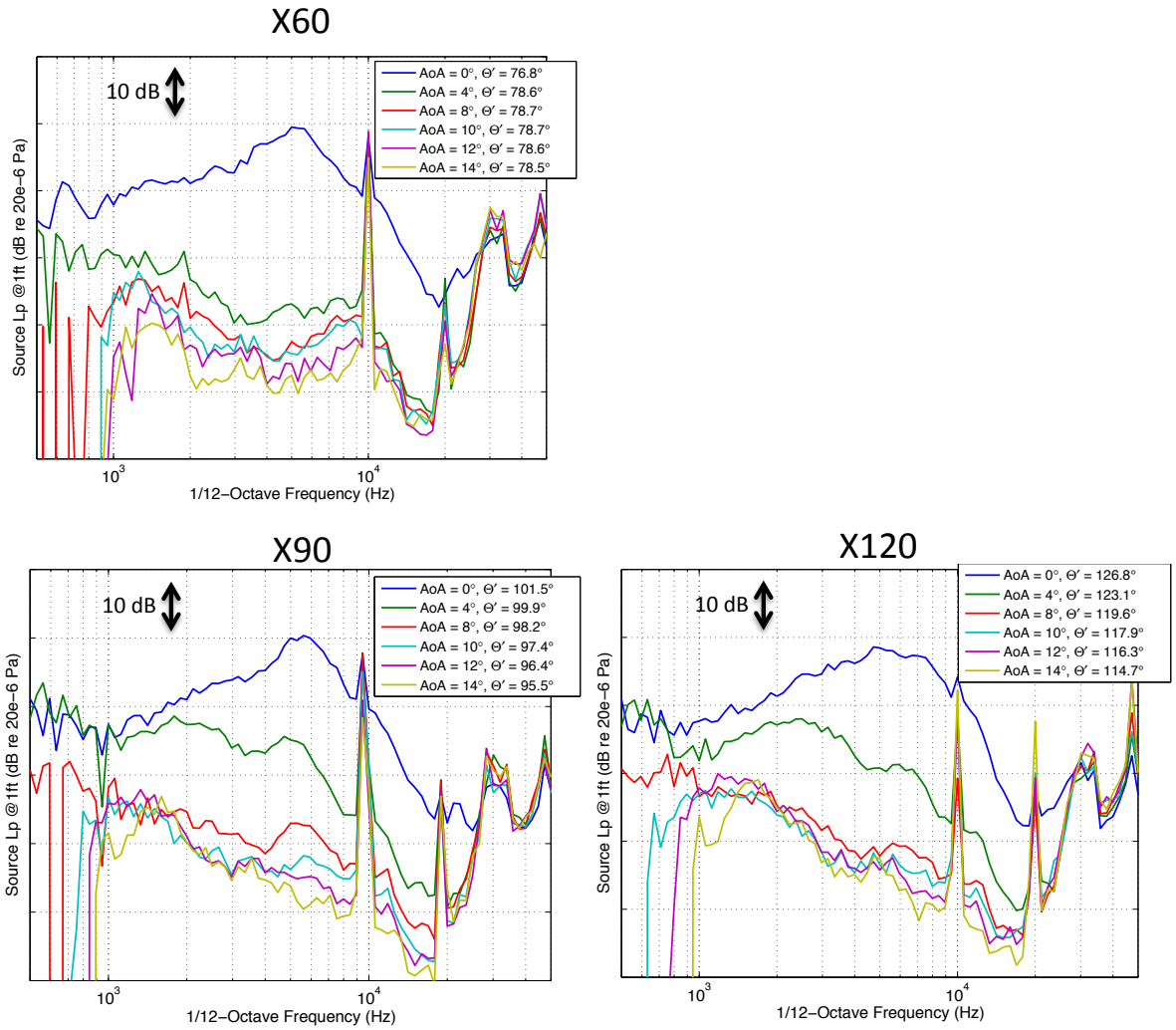

Figure 27. Angle-of-attack dependence for a sealed gap: landing, 50°(3,3), M = 0.2.

F. ROI studies

One advantage of the phased array compared with a traditional single microphone measurement is that the phased array can identify multiple noise sources, and consequently help in the understanding of the noise source physics. In the current study the array is located close to the leading-edge Krueger device and can illustrate the noise contributions from different Krueger elements. Two different ROI sub-region case studies allowed for integration of individual noise sources. Figure 28b shows one dividing method of ROI regions, and Figure 28a shows the corresponding spectrum of each ROI sub-region. It shows that the relative magnitude of gap region (away from bracket) and bracket region (surrounding bracket region) are similar. However, Figure 29b shows another ROI dividing method with the bracket region enlarged and a smaller gap region with the corresponding integrated spectrum shown in Figure 29a. As can be seen, the noise spectrum in the bracket regions is now much more significant than the noise spectrum in the gap region. The conclusion is that the noise sources due to flow interaction with brackets are the dominant noise source, which is different from previous studies. However, caution must be taken with this conclusion because it was shown that for higher angle-of-attack, gap noise can become the dominate

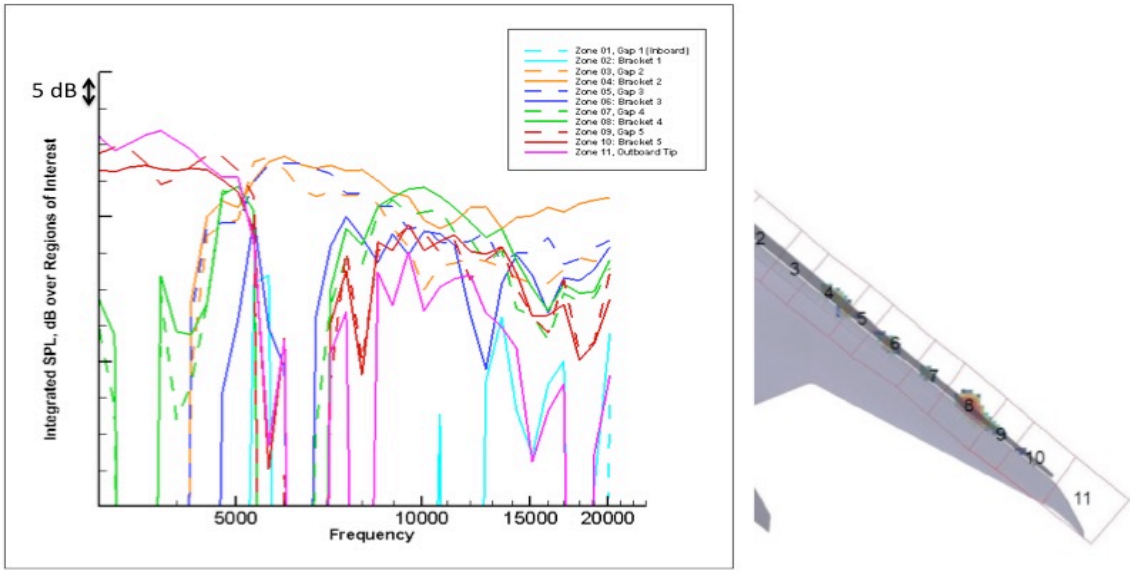

a) Integrated levels for ROI sub-regions. **b) Sub-region definitions.**

Figure 28. ROI sub-region case #1.

noise source. Test day effects such as Kevlar correction and atmospheric attenuation correction were not applied to the sub-ROI studies.

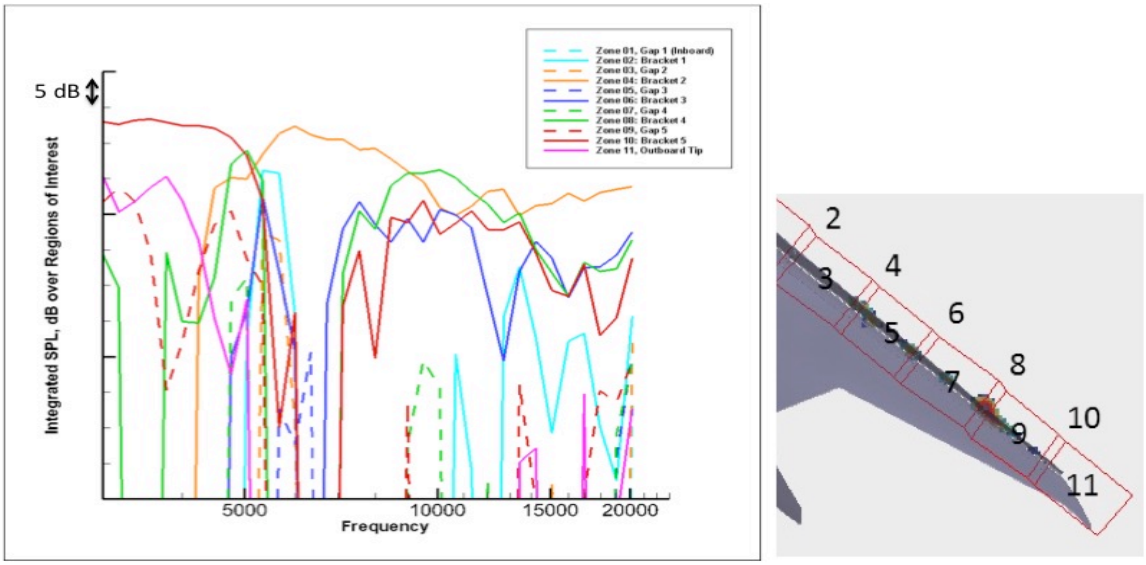

a) Integrated levels for ROI sub-regions. **b) Sub-region definitions.**

Figure 29. ROI sub-region case #2.

VII. Concluding Remarks

A 5.75% Preferred System Concept Hybrid Wing Body vehicle was tested in the AEDC 40- by 80-Foot Wind Tunnel with a traversing phased microphone-array mounted under the left wing. The primary goal of the acoustic

test phase to measure the noise sources associated with the leading-edge Krueger high-lift devices was accomplished. Array resolution was sufficient enough to resolve noise source with 2 inch spacing at most frequencies using DAMAS2 advanced beamforming.

Source emission angles ranging from 60° to 120° showed very little variation in the levels or locations of the Krueger bracket noise sources, which were the dominant noise sources. Inclusion of realistic flight-like brackets illustrated the necessity of correctly modeling the shape, scale, and detail of leading-edge Krueger brackets. Including the additional 17 flight-like brackets increased the leading-edge noise by as much as 5 dB. Sealing the gap between the leading-edge Krueger and the main element reduced the noise at low angle-of-attack but made little difference at approach and landing angles of 14° for a landing configuration with a narrow gap.

Acoustic data acquired during this test will be used to improve noise prediction models of the HWB vehicle and provided value lessons on the fidelity needed for leading-edge high-lift device brackets. With the limited time and funding to develop and execute the acoustic portion of this test the researchers were able to acquire data with exceptionally good spatial resolution. Follow on acoustic testing would ideally include an aerodynamic fairing around the model support strut to further improve the signal-to-noise ratio.

Acknowledgments

This effort was supported by the NASA Environmentally Responsible Aviation Project lead by Fay Collier. Thanks to Kevin James, Sub-Program Manager, Jeffrey Flamm, ITD51 Tech Lead, and Robert Fong, Test Manager. Model graphic software provided by Edward Schairer.

References

[1] Guo, Y., Brusniak, L., Czech, M., Thomas, R.H., "Hybrid Wing Body (HWB) Slat Noise Analysis," 51st AIAA Aerospace Sciences Meeting, AIAA 2013-0462, Grapevine, TX, January 2013.

[2] Horne, W.C., Burnside, N.J., Soderman, P.T., Jaeger, S.M., Reinero, B.R., James, K.D., and Arledge, T.K., "Aeroacoustic Study of a 26%-Scale Semi-Span Model of A Boeing 777 Wing in the NASA Ames 40- by 80-Foot Wind Tunnel", NASA/TP-2004-2128028, Oct. 2004.

[3] Dickey, E.D., Princen, H.P., Bonet, J.T., Ige, G.K., "Wind Tunnel Model Design and Fabrication of a 5.75% Scale Blended-Wing-Body Twin Jet Confiugration," 54th AIAA Aerospace Sciences Meeting, AIAA 2016-XXXX, San Diego, CA, January 2016.

[4] Dougherty, R.P., Aeroacoustic Measurements, Springer-Verlag Berline Heidenlberg, Germany, ed Thomas Mueller, 2002.

[5] Dougherty, R.P., "Functional Beamforming for Aeroacoustic Source Distributions," 20th AIAA/CEAS Aeroacoustics Conference, AIAA 2014-3066, Atlanta, GA, June 2014.

[6] Dougherty, R.P. and Podboy, G.G., "Improved Phased Array Imaging of a Model Jet," 15th AIAA/CEAS Aeroacoustics Conference, AIAA 2009-3186, Miami, FL, May 2009.

[7] Sijtsma, P., "CLEAN Based on Spatial Source Coherence," 13th AIAA/CEAS Aeroacoustics Conference, AIAA2007-3436, Rome, Italy, May 2007.

[8] Dougherty, R.P, "Extensions of DAMAS and Benefits and Limitations of Deconvolution in Beamforming," 11th AIAA/CEAS Aeroacoustics Conference, May 2005, Monterey, CA.

[9] Soderman, P.T., and Allen, C.A., Aeroacoustic Measurements, Springer-Verlag Berline Heidenlberg, Germany, ed Thomas Mueller, 2002.

[10] Jaeger, S.M., Horne, W.C., Allen, C.S., "Effect of Surface Treatment on Array Microphone Self-Noise," 6th AIAA/CEAS Aeroacoustics Conference, AIAA 2000-1937, Lahaina, HI, June 2000.

[11] Shields F.D. and Bass, H.E., "Atmospheric Absorption of High Frequency Noise and Applications to Fractional-Octave Bands," NASA CR 2760, 1977.